Journal Name

COMMUNICATION

Enhancing potassium-ion battery performance by defect and interlayer engineering

Received 00th January 20xx,
Accepted 00th January 20xx

DOI: 10.1039/x0xx00000x

www.rsc.org/

Yang Xu,[†*a] Farzaneh Bahmani,[†ab] Min Zhou,[a] Yueliang Li,[c] Chenglin Zhang,[a] Feng Liang,[d] Sayed Habib Kazemi,[b] Ute Kaiser,[c] Guowen Meng *[e] and Yong Lei *[a]

Defect and interlayer engineering is applied to exploit the large van der Waals gaps of transition metal dichalcogenides for potassium-ion batteries (KIBs). As a demonstrator, MoS_2 nanoflowers with expanded interlayer spacing and defects in basal planes are used as KIB anodes in the voltage range of 0.5-2.5 V, where an intercalation reaction rather than a conversion reaction takes place to store K-ions in the van der Waals gaps. The nanoflowers show enhanced K-storage performance compared to the defect-free counterpart that has pristine interlayer spacing. Kinetic analysis verifies that K-ion diffusion coefficient and surface charge storage are both enhanced in the applied voltage range of intercalation reaction. The collective effects of expanded interlayer spacing and additionally exposed edges induced by the in-plane defects enable facile K-ion intercalation, rapid K-ion transport and promoted surface K-ion adsorption simultaneously.

Introduction

The greater abundance and accessibility of the Na and K resources comparing with the Li resource have prompted researchers to investigate the feasibility of Na-ion and K-ion batteries (KIBs).[1-5] Given the more negative redox potential of K^+ than Na^+ (K^+/K = -2.93 V, Na^+/Na = -2.71 V vs. standard hydrogen electrode), there could be no loss of cell capacity and energy density even though K^+ is bigger than Na^+,[6] making KIBs hold much promise for large-scale stationary energy storage. However, the size of K^+ imposes a major challenge to ion diffusion, often resulting in poor kinetics. This calls for electrode materials with proper structural features that could facilitate K-ion diffusion.

Two-dimensional transition metal dichalcogenides (2D TMDs) have gained world-wide attention in recent years and are being heavily studied in many research domains.[7-10] TMDs possess a unique layered structure characterized by the weak van der Waals interaction between neighboring layers and strong in-plane covalent bonding within each layer. Such uniqueness allows the intercalation of guest species in the interlayer space without significant structural distortion. In this regard, 2D TMDs have been employed as electrode materials in KIBs very recently.[11-13] Hierarchical VS_2 nanosheets assemblies[12] and MoS_2 "nano-rose"@reduced graphene oxide composites[13] displayed some of the best electrochemical performances to date as KIB anodes owing to the architectural and/or compositional features. As we pointed out, the large van der Waals gaps should be ideal for fast 2D K-ion diffusion, but they have not been well exploited because these studies in KIBs focused on high capacity derived from the four-electron reduction reaction that could destroy the gaps as diffusion pathways. Wu et al. observed a stoichiometric K^+ intercalation compound, $K_{0.4}MoS_2$, in commercial MoS_2 power, and demonstrated a cycling stability under this intercalation ratio at the discharge depth of 0.5 V (vs. K^+/K) to ensure the preservation of the van der Waals gaps.[11] Despite the relatively low reversible capacity (~64 mAh g^{-1}) and moderate rate capability (~55 mAh g^{-1} at 160 mA g^{-1}), this work encourages us to fully exploit the van der Waals gaps for K-storage.

The enhancement of K-storage in the van der Waals gaps arises when two criteria are met (Fig. 1): (i) the interlayer spacing is expanded and (ii) the interlayer space becomes more accessible for K-ion to intercalate. On the one hand, interlayer expansion could straightforwardly facilitate K-ion transport because of the reduced transport resistance. On the other hand, making interlayer space more accessible could be achieved by creating defects in the basal planes of the layers, where micro-channels are created to act as K-ion intercalation sites to shorten diffusion distance and open up the inner space between the layers. Moreover, the second point could

[a] Fachgebiet Angewandte Nanophysik, Institut für Physik & ZMN MacroNano (ZIK), Technische Universität Ilmenau, Ilmenau 98693, Germany. Email: yang.xu@tu-ilmenau.de; yong.lei@tu-ilmenau.de
[b] Department of Chemistry, Institute for Advanced Studies in Basic Sciences, Zanjan 45137, Iran.
[c] Central Facility for Electron Microscopy, Electron Microscopy Group of Materials Science, Ulm University, Ulm 89081, Germany.
[d] State Key Laboratory of Complex Nonferrous Metal Resources Clean Utilization, Kunming University of Science and Technology, Kunming 650093, China.
[e] Institute of Solid State Physics, Chinese Academy of Sciences, Hefei, Anhui 230031, China. Email: gwmeng@issp.ac.cn
† These authors contributed equally.
Electronic Supplementary Information (ESI) available: SEM before and after cycling; elemental mapping; XRD after annealing; CV curves; charge/discharge profiles at initial cycles; calculation of D_k; TEM after cycling. See DOI: 10.1039/x0xx00000x

bring extra benefit that the micro-channels could generate additional edges of the layers with additionally exposed edge sites that are known to exhibit fast response to faradaic and non-faradaic processes.[14] Surface K-ion storage and fast kinetics can be expected since edge sites are theoretically and experimentally found to be active for the bonding interaction with ions and molecules.[15-17] Surprisingly, utilization of the edge sites of TMDs is scarce in the studies of ion batteries. It is therefore of great importance to achieve a full exploitation of the van der Waals gaps in 2D TMDs by realizing the above discussed benefits, yet remains challenging to simultaneously expand interlayer spacing, open interlayer space, and create additional edge sites. This shall lead to the enhancement of K-storage in 2D TMDs.

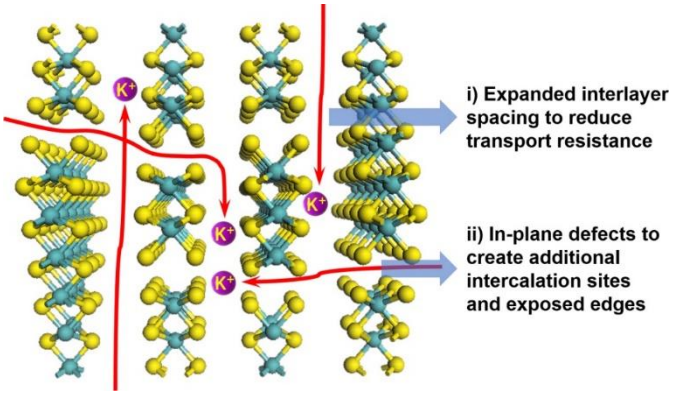

Fig. 1 Illustration of defect and interlayer engineering to enhance KIB performance.

Herein, we highlight a facile defect and interlayer engineering to meet the challenge. We chose MoS_2 as a demonstrator because it has received rapidly increasing attention as a KIB anode material. We obtained interlayer-expanded and defect-rich MoS_2 nanoflowers (D-MoS_2 NFs) by adjusting the ratio between the Mo and S precursors during synthesis. By controlling the working voltage to be 0.5-2.5 V in which intercalation reaction dominates the electrochemical mechanism, we demonstrate the feasibility of enhancing KIB performance through modulating K-storage behavior in the van der Waals gaps. The nanoflowers exhibited a K-intercalation capacity that is 40% higher than the defect-free counterpart with pristine interlayer spacing, and a rate capability of ~50 mAh g^{-1} at 0.8 A g^{-1}. We attribute the enhancement to the increased K-ion diffusivity and surface charge storage, which is enabled by the expanded interlayer spacing and in-plane defects.

Results and discussion

D-MoS_2 NFs were synthesized by reacting ammonium molybdate with excess thiourea through a one-pot hydrothermal reaction, while the defect-free NFs were obtained using the stoichiometric ratio (ESI†). The excess thiourea releases a large amount of ammonia that can be in-situ intercalated into the space between the MoS_2 layers, which is responsible for the expansion of the interlayer spacing. Similar phenomenon was observed in previous work of transition metal dichalcogenides with expanded interlayer spacing.[18,19] The morphology and microstructure of the as-prepared samples were characterized by scanning electron microscopy (SEM) and aberration-corrected transmission electron microscopy (TEM). Fig. S1a and S1c show both samples have a flower-like spherical architecture with a diameter of 2.5-3.5 μm. Fig. S1b and S1d reveal the flowers consist of ultrathin nanosheets with obvious corrugations. The thickness of the nanosheets is estimated to be around 10 nm. High-resolution TEM (HRTEM) images in Fig. 2 give direct depiction of the side and basal planes, showing a typical lamellar structure with curvy edges and a thickness around 10 nm, which is consistent with the SEM observations. An interlayer spacing of 0.91 nm was observed in D-MoS_2 NFs (Fig. 2a), while 0.63 nm was observed in MoS_2 NFs (Fig. 2c), demonstrating a substantial expansion of the interlayer space. The crystal fringes of D-MoS_2 are discontinuous along the curvy edge, forming "cracks" at different locations indicated by the arrows, which is attributed to the rich defects in basal planes.[20,21] A lattice fringe of 0.27 nm, corresponding to the *d* spacing of the (100) plane of MoS_2, can be seen in the basal planes of both samples (Fig. 2b and 2d), suggesting the same atomic orientation along this dimension. However, careful observation reveals that the directions of the (100) fringes of D-MoS_2 NFs are not consistent over the entire basal surface and slightly rotate from one micro-region to another (Fig. 2b), causing lattice fringe distortion as indicated by the circles. The generated defects in the basal planes can cause discontinuity of the sides and additionally exposed edges ("cracks" in Fig. 2a).[17,22] In contrast, more continuous and highly oriented fringes are found in MoS_2 NFs (Fig. 2d). Three-window elemental maps (Fig. S2) acquired in the energy-filtered TEM (EFTEM)[23,24] demonstrate the existence and even distribution of Mo and S in both samples.

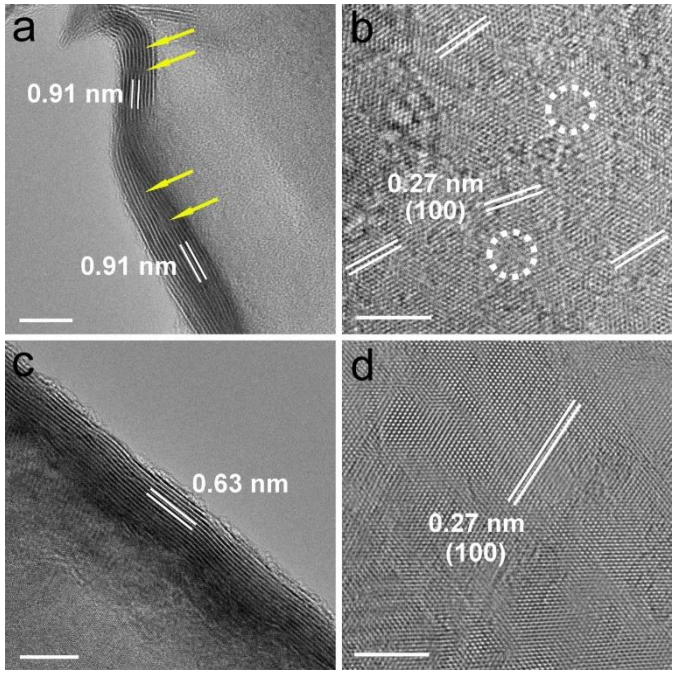

Fig. 2 HRTEM images of the side (a and c) and basal planes (b and d) of D-MoS_2 (a and b) and MoS_2 NFs (c and d). The "cracks" indicated by the arrows in (a) show the discontinuity of the side, implying the rich defects caused by the missing of the atoms. Scale bars: 10 nm (a and c) and 5 nm (b and d).

Fig. 3a shows the X-ray diffraction (XRD) patterns that can be well indexed to hexagonal MoS_2 (JCPDS 37-1492). Peak broadening

implies a small number of stacked layers as observed in Fig. 2a and 2c. A shift of (002) peak from 14.4° in the standard pattern to 14.0° in the experimental patterns indicates an increased interlayer spacing to 0.63 nm, which agrees with other reported nanosized MoS_2.[25,26] D-MoS_2 NFs show another peak located at 9.7° that corresponds to the substantially expanded interlayer spacing of 0.91 nm that is observed in Fig. 2a. A second-order (004) diffraction peak appears between 17° and 19°, which could be probably ascribed to the ammonia intercalating in the interlayer space.[18,27] After annealed at 700°C, the absence of both peaks indicates ammonia is expelled from the interlayer space, resulting in the conversion to the thermodynamically stable structure and the restoration to the spacing of 0.63 nm (Fig. S3). This provides an auxiliary support of the expanded spacing at the as-prepared condition.[20] Two broadened peaks at 32° and 57° can be indexed to (100) and (110) planes of MoS_2, respectively, once again indicating the two samples have the same atomic orientation along the basal planes. It is worth noting that D-MoS_2 exhibits more broadened (100) and (110) peaks than MoS_2, which is attributed to the more disordered crystal structure caused by the in-plane defects, as seen in Fig. 2b where the defects induce many nanodomains in the basal planes. Raman spectra (Fig. 3b) show the peaks located at 381.6 and 407.1 cm^{-1} which are attributed to the planar (E^1_{2g}) and out-of-plane (A_{1g}) vibration modes of MoS_2, respectively,[13,28] further demonstrating the phase purity of the samples. As shown in the spectra of X-ray photoelectron spectroscopy (XPS, Fig. 3c and 3d), the peaks at 228.5 and 231.7 eV are assigned to Mo $3d_{5/2}$ and $3d_{3/2}$ of Mo^{4+}, respectively, and those at 161.3 and 162.5 eV are assigned to S $2p_{3/2}$ and $2p_{1/2}$ of S^{2-}, respectively. The lowered binding energies by 0.4~0.5 eV in D-MoS_2 NFs imply their enlarged interlayer spacing.[29] The atomic ratio of S:Mo is 1.89 and 1.77 for D-MoS_2 and MoS_2 NFs, respectively. Previous study reported metal edge with unsaturated S coverage is the most stable structure among differently exposed edges, which results in a higher content of S.[30] The obtained ratio hints D-MoS_2 NFs have more exposed Mo-S edges caused by the defects in basal planes. The combined analysis of phase, composition, morphology and microstructure prove the expanded interlayer spacing and defects as well as the additionally exposed edges in D-MoS_2 NFs. These features are expected to facilitate K-ion intercalation/diffusion and increase surface K-ion adsorption, leading to the enhancement of K-storage in the van der Waals gaps.

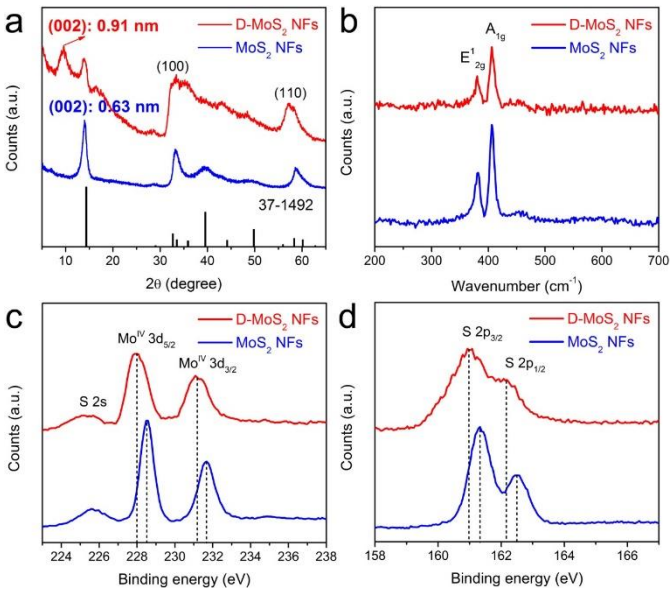

Fig. 3 XRD patterns (a), Raman spectra (b), Mo 3d XPS spectra (c), and S 2p XPS spectra (d) of D-MoS_2 and MoS_2 NFs.

Prior to test batteries, it is critical to ensure that no crystal reconstruction caused by conversion reaction occurs upon K-ion intercalation/de-intercalation because the reconstruction could destroy the van der Waals gaps as K-ion diffusion pathway. Previous studies showed that Na intercalation in MoS_2 occurs at a voltage above 0.4 V (vs. Na^+/Na), beyond which intercalation is replaced by conversion and the layered structure collapses.[25,31,32] A recent work of KIBs showed 0.5 V (vs. K^+/K) to be a suitable discharge depth at which only intercalation occurs.[11] Accordingly, we chose a voltage range of 0.5-2.5 V in this work. Fig. 4 shows the XRD patterns of the two samples recorded after the first discharge and charge processes. All the patterns show the characteristic (002), (100), and (110) peaks of the layered structure, and no peaks of Mo or K_2S were detected. The peak located at 9.7° remains after cycling D-MoS_2 NFs. The results prove that only intercalation reaction occurs and both samples maintain the layered structure.

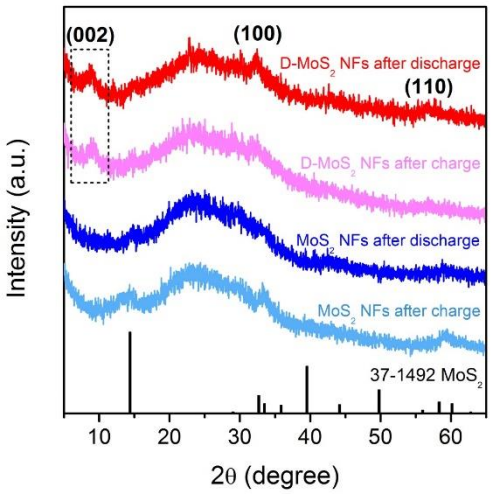

Fig. 4 XRD patterns of D-MoS_2 and MoS_2 NFs after discharge and charge at the current density of 50 mA g^{-1}. The broad peak between 20° and 30° is attributed to super P which is used as conductive additive in the electrodes.

With the above prerequisite established, we tested batteries to verify the defect and interlayer engineering for fully exploiting the van der Waals gaps towards enhanced KIB performance. Fig. S4 and 5a show the discharge-charge profiles at cycle1, 2 and 100. MoS_2 NFs have an initial discharge plateau around 1.15 V, followed by a quasi-plateau centered at 0.75 V before reaching the cutoff voltage. At cycle2, the discharge plateau shifts to a slightly higher voltage and becomes less defined, while the charge curve remains unchanged. For the case of D-MoS_2, a slope replaces the plateau during discharge at cycle1 and remains at cycle2. Both samples display sloping curves at cycle100 (Fig. 5a). The observed results agree with the cyclic voltammetry (CV) profiles shown in Fig. S5. The cycle1 discharge/charge capacities are 280/104 mAh g^{-1} for D-MoS_2 NFs and 225/77 mAh g^{-1} for MoS_2 NFs, giving relatively low initial Coulombic efficiencies (CEs) of 37 and 34%, respectively. This is most likely due to the decomposition of the electrolyte and the formation of solid-

electrolyte interface (SEI). We tested a control battery using only the conductive additive and binder, and it showed a lower initial CE of 16% (Fig. S6). As shown in Fig. 5b, the CE of D-MoS_2 NFs reaches 90% at cycle4, comparing with cycle7 for MoS_2 NFs. D-MoS_2 NFs delivered a reversible capacity of 94 mAh g^{-1} at cycle100, being 40% higher than that of MoS_2 NFs (67 mAh g^{-1}). To the best of our knowledge, the presented K-intercalation capacity is higher than the previously reported numbers of MoS_2 in KIBs and even comparable to some Na-intercalation capacities.[11,25,31,33] The results show the necessity to control the electrochemical mechanism to be dominated by intercalation reaction in order to make full use of the van der Waals gaps. Rate performance is shown in Fig. 5c. D-MoS_2 NFs exhibited higher capacities than MoS_2 NFs at all testing rates. They delivered reversible capacities of 90, 75, 61, and 48 mAh g^{-1} at 100, 200, 400, and 800 mA g^{-1} (at cycle13, 18, 23, and 28), in comparison with 65, 47, 33, 22 mAh g^{-1} of MoS_2 NFs at the corresponding rate. The capacity of D-MoS_2 NFs was fully recovered to 104 mAh g^{-1} when the current density was reduced back to 50 mA g^{-1}. Stable discharge-charge profiles of D-MoS_2 NFs were obtained at all rates (Fig. 5d). The results show the benefits of the defect and interlayer engineering in MoS_2. First, the expanded interlayer spacing kinetically facilitates the K-intercalation into and K-diffusion within the van der Waals gaps. The "cracks" provide additional ion intercalation sites, as D-MoS_2 NFs show smaller discharge/charge polarization than MoS_2 NFs in the prolonged cycles. The faster increased CE of D-MoS_2 NFs during the initial cycles signals a higher reversibility owing to the less trapped K-ions between the layers.[34,35] Second, the additionally exposed edges provide extra active sites to adsorb K-ions and increase surface charge storage. It can be evidenced by the more sloping voltage profiles of D-MoS_2 NFs, which may originate from a distribution of adsorption energy.[36,37]

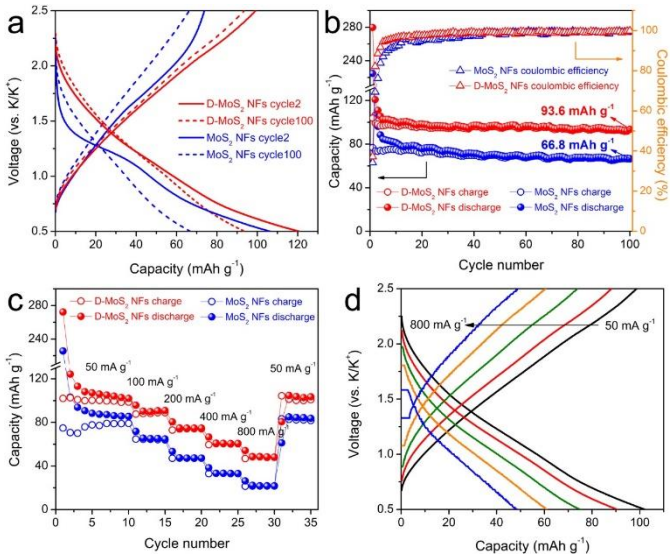

Fig. 5 (a) Discharge-charge profiles at cycle2 and cycle100. (b) cycling performance. (c) Rate capability. (d) Discharge-charge profiles of D-MoS_2 NFs at various current densities.

We next sought to the understanding of the defect and interlayer engineering by using two electrochemical characterization techniques. The first one is galvanostatic intermittent titration (GITT) that can evaluate the K-ion diffusion coefficient (D_k) during potassiation. Fig. 6a shows the potential response, where the potential change during each relaxation period represents the overpotential at the corresponding potassiation stage.[38] D-MoS_2 NFs exhibited much smaller overpotentials than MoS_2 NFs in the entire potential range, which implies a better kinetic property. The linearity of the potential change with the square root of the relaxation time is shown in Fig. S7 and the calculation of D_k is shown in Fig. S8. Fig. 5b shows the values of D_k as a function of potential. Both samples displayed a progressively decreasing D_k with the potassiation proceeding toward cut-off voltage, which agrees with previous literature.[39,40] However, the D_k of D-MoS_2 NFs is much higher than that of MoS_2 NFs, especially in the low-voltage region, being in accordance with the smaller overpotentials. This indicates K-diffusion is much faster in D-MoS_2 NFs owing to the expanded interlayer spacing and additional intercalation sites through the "cracks" that make interlayer space easily accessible for K-ions. The second characterization technique is CV. Fig. 6c and S9 show the curves of D-MoS_2 and MoS_2 NFs recorded at the scan rates of 0.1~1 mV s^{-1}, respectively. For the case of D-MoS_2 NFs, broad (de)potassiation peaks are maintained at high scan rates, and the peak separation hardly changes, signaling a very small polarization. For the case of MoS_2 NFs, peaks become steeper and large polarization can be seen. These observations once again indicate the better kinetic property of D-MoS_2 NFs. We used the relationship of peak current (i) and scan rate (v) to analyze the charge storage process according to the equation of $i=av^b$, where the b value can be extracted from the slope by plotting log(i) against log(v). It is 0.5 for an ideal faradiac intercalation process controlled by semi-infinite linear diffusion while close to 1 for a surface charge storage process free of diffusion control.[41,42] A good linear relationship can be seen in both samples (Fig. 6d). D-MoS_2 NFs show the b values of 0.94 and 0.86 for the anodic and cathodic processes, respectively, and both are higher than those of MoS_2 NFs (0.74 and 0.76). The comparison suggests that the K-storage is less diffusion controlled in D-MoS_2 NFs, which can be ascribed to the active sites that could adsorb more K-ions on the additionally exposed edges, resulting in faster kinetics.

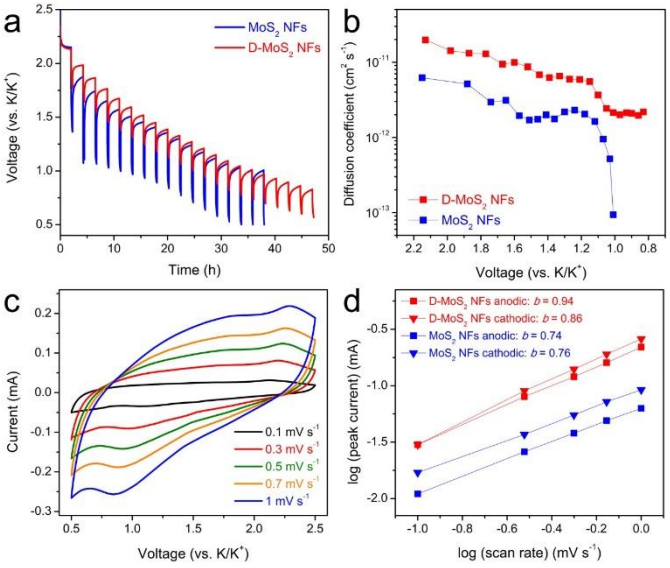

Fig. 6 (a) GITT profiles of the discharge process. (b) D_k as a function of the state of the discharge process. (c) CV curves of D-MoS_2 NFs at various scan rates. (d) b-value determination.

Therefore, our electrochemical characterizations demonstrate that the kinetic property of MoS_2 can be greatly improved by the expansion of interlayer spacing and exposure of additional edges. The presented material engineering not only facilitates K-intercalation and diffusion but also promotes surface K-storage, leading to the full exploitation of the van der Waals gaps.

We further characterized the morphology and structure of the samples after 100 cycles. The nanosheet morphology can be seen (Fig. S10a and S10b), despite the contour of the sheets is less defined due to the SEI layer. The preservation of the sheet-like shape indicates (de)intercalation process has minimal damage to the microstructures of the MoS_2 NFs, once again suggesting the preservation of the van der Waals gaps. HRTEM images (Fig. S10c and S10d) show both samples have more expanded layers comparing with their original states, but the layers arrange more ordered in D-MoS_2 NFs than in MoS_2 NFs, which can be attributed to the better K-diffusion kinetic in the former. Nevertheless, the layered structure was kept intact with the cut-off voltage of 0.5 V, demonstrating a high structural reversibility during K-storage. It is very different from the conversion mechanism that has been popularly employed for ion-storage in MoS_2, with a cut-off voltage of 0.1 V or lower, to reach a high capacity. The generation of Mo and metal sulfide destroys the layered structure and rebuilding the structure is difficult to be reversible, as evidenced by the detection of the Mo and sulfide phases after charging process.[43,44] The destroy of the layered structure often leads to severe capacity decay, thus incorporation of structure support and conductivity enhancer, e.g. carbon materials, was involved in almost all the previous literature of MoS_2.[13,45-48] Our work supports defect engineering as a new perspective to balance capacity and structural stability when designing electrode materials in KIBs.

Conclusions

In summary, taking MoS_2 nanoflowers as an example, we demonstrate the crucial role of defect and interlayer engineering in 2D TMDs for exploiting the van der Waals gaps and enhancing KIB performance. The presented engineering creates expanded interlayer spacing and in-plane defects that leads to the exposure of additional edges of MoS_2. As a result, facile K-ion intercalation, rapid K-ion transport and promoted surface K-ion storage are obtained simultaneously. The benefits were verified by a series of measurements, including long-term cycling, rate capability, GITT, and CV. The success of applying defect and interlayer engineering may pave the way towards a more efficient utilization of the prominent structural features of electrode materials, e.g., 2D diffusion pathways and lamellar structures. Significant improvement of KIBs can be expected by designing materials with defect-rich structures, and it may open new possibilities of using defects in other energy storage systems.

Conflicts of interest

There are no conflicts to declare.

Acknowledgements

This work was financially supported by the European Research Council (ThreeDsurface, 240144, and HiNaPc, 737616), BMBF (ZIK-3DNanoDevice, 03Z1MN11), and German Research Foundation (DFG: LE 2249/4–1 and LE 2249/5-1).

References

1 N. Yabuuchi, K. Kubota, M. Dahbi and S. Komaba, *Chem. Rev.*, 2014, **114**, 11636-11682.
2 Y. Xu, M. Zhou and Y. Lei, *Adv. Energy Mater.*, 2016, **6**, 1502514.
3 Y. Xu, M. Zhou and Y. Lei, *Materials Today*, 2018, **21**, 60-78.
4 J. C. Pramudita, D. Sehrawat, D. Goonetilleke and N. Sharma, *Adv. Energy Mater.*, 2017, **7**, 1602911.
5 L. Wen, Z. Wang, Y. Mi, R. Xu, S. Yu and Y. Lei, *Small*, 2015, **11**, 3408-3428.
6 L. Xue, H. Gao, W. Zhou, S. Xin, K. Park, Y. Li and J. B. Goodenough, *Adv. Mater.*, 2016, **28**, 9608-9612.
7 S. Manzeli, D. Ovchinnikov, D. Pasquier, O. V. Yazyev and A. Kis, *Nat. Rev. Mater.*, 2017, **2**, 17033.
8 X. Chia, A. Y. S. Eng, A. Ambrosi, S. M. Tan and M. Pumera, *Chem. Rev.*, 2015, **115**, 11941-11966.
9 J. Xu, J. Zhang, W. Zhang and C. S. Lee, *Adv. Energy Mater.*, 2017, **7**, 1700571.
10 H. Zhu, C. Xiao, H. Cheng, F. Grote, X. Zhang, T. Yao, Z. Li, C. Wang, S. Wei, Y. Lei and Y. Xie, *Nature Commun.*, 2014, **5**, 3960.
11 X. Ren, Q. Zhao, W. D. McCulloch and Y. Wu, *Nano Res.*, 2017, **10**, 1313-1321.
12 J. Zhou, L. Wang, M. Yang, J. Wu, F. Chen, W. Huang, N. Han, H. Ye, F. Zhao and Y. Li, *Adv. Mater.*, 2017, **29**, 1702061.
13 K. Xie, K. Yuan, X. Li, W. Lu, C. Shen, C. Liang, R. Vajtai, P. Ajayan and B. Wei, *Small*, 2017, **13**, 1701471.
14 R. L. McCreery, *Chem. Rev.*, 2008, *108*, 2646-2687.
15 Y. Li, D. Wu, Z. Zhou, C. R. Cabrera and Z. Chen, *J. Phys. Chem. Lett.*, 2012, **3**, 2221-2227.
16 H. He, J. Lin, W. Fu, X. Wang, H. Wang, Q. Zeng, Q. Gu, Y. Li, C. Yan and B. K. Tay, *Adv. Energy Mater.*, 2016, **6**, 1600464.
17 G. Ye, Y. Gong, J. Lin, B. Li, Y. He, S. T. Pantelides, W. Zhou, R. Vajtai and P. M. Ajayan, *Nano Lett.*, 2016, **16**, 1097-1103.
18 Q. Liu, X. Li, Z. Xiao, Y. Zhou, H. Chen, A. Khalil, T. Xiang, J. Xu, W. Chu, X. Wu, J. Yang, C. Wang, Y. Xiong, C. Jin, P. M. Ajayan, L. Song, *Adv. Mater.*, 2015, **27**, 4837-4844.
19 M. Gao, M. K.Y. Chen, Y. Sun, *Nature Commun.*, 2015, **6**, 7493.
20 J. Xie, J. Zhang, S. Li, F. Grote, X. Zhang, H. Zhang, R. Wang, Y. Lei, B. Pan and Y. Xie, *J. Am. Chem. Soc.*, 2013, **135**, 17881-17888.
21 S. Zhang, X. Yu, H. Yu, Y. Chen, P. Gao, C. Li and C. Zhu, *ACS Appl. Mater. Interfaces*, 2014, **6**, 21880-21885.
22 J. Xie, H. Zhang, S. Li, R. Wang, X. Sun, M. Zhou, J. Zhou, X. W. D. Lou and Y. Xie, *Adv. Mater.*, 2013, **25**, 5807-5813.
23 C. Jeanguillaume, P. Trebbia and C. Colliex, *Ultramicroscopy*, 1978, **3**, 237-242.
24 R. F. Egerton, *Electron Energy-Loss Spectroscopy in the Electron Microscopy*, Plenum Press, New York, 1996.
25 J. B. Cook, H. S. Kim, Y. Yan, J. S. Ko, S. Robbennolt, B. Dunn and S. H. Tolbert, *Adv. Energy Mater.*, 2016, **6**, 1501937.
26 X. Wang, X. Shen, Z. Wang, R. Yu and L. Chen, *ACS Nano*, 2014, **8**, 11394-11400.
27 Y. Xu, L. Wang, X. Liu, S. Zhang, C. Liu, D. Yan, Y. Zeng, Y. Pei, Y. Liu, S. Luo, *J. Mater. Chem. A*, 2016, **4**, 16524-16530.
28 T. S. Sahu and S. Mitra, *Sci. Rep.*, 2015, **5**, 12571.
29 X. Wang, Z. Guan, Y. Li, Z. Wang and L. Chen, *Nanoscale*, 2015, **7**, 637-641.

30 D. Chao, P. Liang, Z. Chen, L. Bai, H. Shen, X. Liu, X. Xia, Y. Zhao, S. V. Savilov and J. Lin, *ACS Nano*, 2016, **10**, 10211-10219.
31 J. Park, J.-S. Kim, J.-W. Park, T.-H. Nam, K.-W. Kim, J.-H. Ahn, G. Wang and H.-J. Ahn, *Electrochimica Acta*, 2013, **92**, 427-432.
32 Q. Li, Z. Yao, J. Wu, S. Mitra, S. Hao, T. S. Sahu, Y. Li, C. Wolverton and V. P. Dravid, *Nano Energy*, 2017, **38**, 342-349.
33 S. Wang, J. Tu, Y. Yuan, R. Ma and S. Jiao, *Phys. Chem. Chem. Phys.*, 2016, **18**, 3204-3213.
34 E. M. Lotfabad, P. Kalisvaart, A. Kohandehghan, D. Karpuzov and D. Mitlin, *J. Mater. Chem. A*, 2014, **2**, 19685-19695.
35 M. Zhou, Y. Xu, C. Wang, Q. Li, J. Xiang, L. Liang, H. Zhao, M. Wu and Y. Lei, *Nano Energy*, 2017, **31**, 514-524.
36 H. Wang, D. Mitlin, J. Ding, Z. Li and K. Cui, *J. Mater. Chem. A*, 2016, **4**, 5149-5158.
37 J. Hou, C. Cao, F. Idrees and X. Ma, *ACS Nano*, 2015, **9**, 2556.
38 Y. Xu, Y. Zhu, Y. Liu and C. Wang, *Adv. Energy Mater.*, 2013, **3**, 128.
39 Z. Jian, Z. Xing, C. Bommier, Z. Li and X. Ji, *Adv. Energy Mater.*, 2016, **6**, 1501874.
40 P. Bonnick, X. Sun, K.-C. Lau, C. Liao and L. F. Nazar, *J. Phys. Chem. Lett.*, 2017, **8**, 2253-2257.
41 T. Brezesinski, J. Wang, S. H. Tolbert and B. Dunn, *Nat. Mater.*, 2010, **9**, 146-151.
42 V. Augustyn, J. Come, M. A. Lowe, J. W. Kim, P.-L. Taberna, S. H. Tolbert, H. D. Abruña, P. Simon and B. Dunn, *Nat. Mater.*, 2013, **12**, 518-522.
43 J. Wang, C. Luo, T. Gao, A. Langrock, A. C. Mignerey and C. Wang, *Small*, 2015, **11**, 473-481.
44 X. Fang, C. Hua, X. Guo, Y. Hu, Z. Wang, X. Gao, F. Wu, J. Wang and L. Chen, *Electrochimica Acta*, 2012, **81**, 155-160.
45 W. Ren, H. Zhang, C. Guan and C. Cheng, *Adv. Funct. Mater.*, 2017, **27**, 1702116.
46 X. Xie, T. Makaryan, M. Zhao, K. L. Van Aken, Y. Gogotsi and G. Wang, *Adv. Energy Mater.*, 2016, **6**, 1502161.
47 Z. Li, A. Ottmann, T. Zhang, Q. Sun, H.-P. Meyer, Y. Vaynzof, J. Xiang and R. Klingeler, *J. Mater. Chem. A*, 2017, 5, 3987-3994.
48 Y. Liu, X. He, D. Hanlon, A. Harvey, U. Khan, Y. Li and J. N. Coleman, *ACS Nano*, 2016, **10**, 5980-5990.

